Summer 8-13-2020

First-Principles Investigation of Doping and Alloying of β-Ga2O3

Ben Tattersfield
Washington University in St. Louis

Washington University in St. Louis

McKelvey School of Engineering

Department of Materials Science and Engineering

Thesis Examination Committee:

Rohan Mishra, Chair

Katharine Flores

Chuan Wang

First-principles investigation of doping and alloying of β-Ga_2O_3

By

Benjamin Ryan Tattersfield

A thesis presented to the McKelvey School of Engineering of Washington University in St. Louis in partial fulfillment of the requirements for the degree of Master of Science

August 2020

St. Louis, Missouri

Acknowledgements

This thesis represents the culmination of a long educational adventure that bears little resemblance to the one I had at first envisioned. Some of the trajectory changes along this path were the result of profoundly negative events, the disruption caused by the COVID-19 pandemic being principle among them. But many and more of the adjustments to my educational trajectory were the result positive perturbations, the movers of which I would like to take this opportunity to acknowledge.

I would like to acknowledge the influence of my first physics educator, Wilson Hubbell, who catalyzed my interest in learning "to solve novel problems" which makes up the crux of engineering thinking. His enlightened teaching approach sharply raised my expectations for collegiate education and directly led to my pursuit of an engineering degree.

My Bates College advisor, Gene Clough, guided me to the engineering dual-degree program, for which I am immeasurably grateful.

My WashU advisor, Rohan Mishra, gave me my first exposure to the wonderful and fascinating field of Materials Science, and I've never looked back. His guidance is inextricably entangled with the content of this thesis, and no part of it would have been possible without him.

My sincerest thanks to John Cavin, my indefatigable reviewer who, frankly, would have been more than justified if he'd said: "no, not this time. Ask someone else" at least once.

To all of the other members of the MCube group, whose intellects and insights have been invaluable along the way as examples and resources, I offer my thanks.

Innumerable friends and mentors have supported me along the way here, each with their own unique contribution to my work and development as a person. I dare not try for an exhaustive list, because of the risk of my forgetfulness leading to omission of anyone. My thanks to all of them.

A hearty thanks to my extended family for their support throughout my education, even if they didn't understand what I was saying, conservatively estimating, 101% of the time.

A shoutout to Claire and Maggie, my sisters. For some reason, they seem to think that I have my act together. Their blind confidence in me might be the reason that I ever do.

A final and comprehensive thanks to my parents George and Margie Tattersfield. They supported me through this educational journey in all conceivable ways. Much love to both of you.

Table of Contents

List of Figures

Abstract

First-principles investigation of doping and alloying of β-Ga_2O_3

By

Benjamin Ryan Tattersfield

Master of Science in Materials Science and Engineering

Washington University in St. Louis, 2020

Research Advisor: Professor Rohan Mishra

β-Ga_2O_3 is an emergent semiconductor for power electronics applications. It has a wide band gap of 4.8 eV and is transparent on the whole spectrum of visible light up to deep ultraviolet. It has a high Baliga figure of merit (BFOM) — a weighted numerical combination of the dielectric constant, charge carrier mobility, and critical breakdown field —, which is commonly used for a quantitative comparison of semiconductors for high-current operation and power switching applications. β-Ga_2O_3 can be grown as thin films or as large single crystals by melt growth-techniques, which is important for scalable manufacturing. However, β-Ga_2O_3 suffers from a lack of *p*-type dopants and a low thermal conductivity. Presently, all applications are based on *n*-type β-Ga_2O_3; the introduction of *p*-type β-Ga_2O_3 would enable bipolar power devices. Additionally, high-power switching results in elevated temperatures where heat retention can impede electronic performance.

The objective of this thesis is to investigate, using first-principles density-functional-theory calculations: (1) the efficiency of doping with Bi to raise the valence band of β-Ga_2O_3 to a level at which *p*-type doping is achievable, and (2) the possibility of

improving the thermal properties of β-Ga_2O_3 by alloying with the lightest Group-13 cation, B.

We find that doping with Bi creates mid-gap states derived from the Bi 6*s* electrons at similar energy level to candidate acceptors through an anti-bonding hybridization of the Bi lone pair with the O 2*p* states. The associated states are more dispersed than the pristine valence band, as they derive from the delocalized *s*-states of Bi rather than the *p*-states of highly electronegative O, which dominate the valence band. Our calculations indicate that these intermediate states are natively filled, and at an appropriate energy level to use a co-dopant like Mg, N, or even native Ga vacancies as *p*-type dopants.

We explored several pathways to include B as an alloy in β-Ga_2O_3, including the high-entropy alloy (HEA) approach and a variety of ordered binary and ternary alloys. Despite these efforts, we do not find a stable alloy, since the small B atoms reject the octahedral and tetrahedral coordination of the cations in β-Ga_2O_3 in favor of a flat triangular coordination, as observed in B_2O_3. We conclude that B is likely insoluble in β-Ga_2O_3 at concentrations high enough to substantively improve its thermal conductivity.

Chapter 1: Introduction

Semiconductors are among the most important materials in the modern era, as they are the operative materials in electronics. These materials enable logic electronics like *p*-*n* junctions and transistors, which drive the computing era. Behaviorally, what makes these materials work this way is the existence of a band gap between electron valence energy levels and the conduction energy levels, which the material's electrons can only occupy under excitations. In contrast to metals, which have continuous electronic energy levels that allow for ready conduction of electrons, this band gap must be overcome with an adequate input of energy bias in order for the valence electrons to make the leap to the conduction bands. This phenomenon has been exploited to world-changing effect, enabling the modern computing era.

Si is the most prevalent semiconductor and is used to make a wide variety of devices on an ever-shrinking length scale. As Si-based devices approach the lowest limits of resolution, research has shifted focus to more diverse materials with different property combinations. Among these alternate materials are wide-gap semiconductors, which are characterized by a band gap wider than 2 eV (bulk Si has a band gap of around 1.1eV [1]). Wide-gap semiconductors are used for high-power and high-frequency electronics, among other applications. This type of material offers a wider range of desirable properties for devices than Si alone. In our work, we focus on β-Ga_2O_3. This material had been considered as a candidate material for Transparent Conducting Oxide (TCO) applications — materials which combine conductive properties with transparency to visual light, a combination which is not possible with opaque Si or with non-conducting amorphous glasses. However, focus has since shifted to using β-Ga_2O_3 for high-power

electronics, where it shows great promise. This thesis reports our use of computational materials science techniques to try to predict mechanisms by which to expand on the present set of demonstrated properties of β-Ga_2O_3.

Chapter 2 of this thesis gives an overview of the computational materials science methods which we use to obtain our results. This begins with the first-principles atomistic modeling method known as Density Functional Theory (DFT), which is derived from fundamental quantum mechanical equations. I briefly discuss the derivation of the theory and list its specific advantages and shortcomings. The other principle method used in this thesis is Special Quasirandom Structures (SQS), which are a random dispersion of atoms that simulates the local disorder of a real alloy. These are used to randomly disperse the atoms in our models, so that we can expediently form structures that give representative results for the actual randomness of a real material.

One of the limits to usage of β-Ga_2O_3 arises from the deep level of valence bands comprised of the highly electronegative O-atoms, which has confounded efforts to dope β-Ga_2O_3 *p*-type. Conclusive demonstration of *p*-type doping would allow β-Ga_2O_3 homostructural *p*-*n* junctions, enabling use of the material for the same types of logic electronics that are the foundation of the computer era. On a more general note, the deep level of O bands has hindered the development of *p*-type doping strategies for other wide-gap oxide semiconductors beyond β-Ga_2O_3. Any successful strategy, properly understood, could provide avenues to *p*-type doping for other important functional oxides. Chapter 3 reports our study of enabling *p*-type doping through elevation of the valence band by doping with Bi.

The other chief obstacle for the widespread use of β-Ga_2O_3 is its poor thermal conductivity. Heat retention has negative implications for device functionality, particularly in high-power or high-frequency operation. In semiconductors, the chief conductors of heat are structural lattice phonons; the retention of heat is associated with a large number of phonon branches, and the low symmetry of β-Ga_2O_3 correlates to a large number of phonon branches. A possible way to address this issue is to lower the mean atomic mass of the elements in the compound, which reduces the average inertial resistance of the atoms in the crystal to lattice vibrations. Chapter 4 presents our study of alloying with lighter Group-13 cations to improve the thermal properties of β-Ga_2O_3.

Chapter 5 compiles our findings and discusses the opportunities associated with them. It includes some speculation on what steps could be taken in future to improve on the work reported in the previous two chapters.

Chapter 2: Methods

Density-Functional Theory Calculations

All of the results in this thesis are based on Density-Functional Theory (DFT) [2,3] calculations performed using the Vienna Ab-Initio Simulation Package (VASP) [4,5]. This section provides a brief description of the underlying physics of DFT and the basics of its implementation. We begin with the mathematical description of an electron, then discuss the derivation of DFT principles from that first-principles description. The implementation of DFT is given some background, with particular focus on the simplifying assumptions made in order to elucidate the subtleties of the method. This section is meant as a conceptual review, rather than a restatement of DFT proofs. As such, most of the underlying mathematical expressions are excluded, as they are not of particular importance to understanding our results. Special attention is paid to explaining the methods for which reporting of the calculation details is necessary for reproduction of the results.

Quantum Mechanical Equations

An electron exhibits properties of both a wave and a particle. It can be diffracted like electromagnetic radiation [6-8], but it also has measurable mass (corpuscular property) [9]. These two behaviors were unreconcilable until early in the 20th century, when the wave-particle duality was proposed by Louis de Broglie [10]. Erwin Schrödinger captured the wave-like nature of non-relativistic electrons in his now-famous partial differential equation:

$$i\hbar \frac{\mathrm{d}}{\mathrm{d}t}\Psi(\boldsymbol{r},t) = \hat{H}\Psi(\boldsymbol{r},t). \quad (1)$$

here, i and $\hbar$ are the imaginary constant and reduced Planck constant respectively, $\widehat{H}$ is a differential operator corresponding to energy known as a Hamiltonian, and Ψ is the wavefunction that accounts for the wave-like nature of the electron [11]. The time-independent version of this equation is an eigenvalue problem expressed as:

$$\widehat{H}\psi(\boldsymbol{r}) = E\psi(\boldsymbol{r}) \tag{2}$$

where ψ and E are an eigenvector-and-eigenvalue solution, respectively, representing a stationary state and its energy. The significance of this time-independent version is that any wavefunction can be decomposed into these wave-like stationary states, thus enabling even a "frozen" electron to mathematically retain its wave-like nature.

The wavefunction approach is not limited to electrons, and can be applied to any system of non-relativistic particles. The key to applying the Schrödinger equation to a system is finding the classical energy of a system as a function of component positions and momenta, $H(\boldsymbol{r}, \boldsymbol{p})$, and making the following replacements to the classical momentum equation to get the Hamiltonian operator, $\widehat{H}$:

$$\boldsymbol{r} \to \boldsymbol{r}, \boldsymbol{p} \to i\hbar\boldsymbol{\nabla} \tag{3}$$

As an example, the transformation from classical-momentum form to quantum-Hamiltonian form is made for a simple harmonic oscillator to a free electron below:

$$\frac{1}{2m}\boldsymbol{p}^2 \to -\frac{\hbar^2}{2m}\boldsymbol{\nabla}^2 \tag{4}$$

A more complete description of the particle momentum would be given like so:

$$\frac{1}{2m}\boldsymbol{p}^2 + \frac{1}{2}m\omega^2\boldsymbol{r}^2 \to -\frac{\hbar^2}{2m}\boldsymbol{\nabla}^2 + \frac{1}{2}m\omega^2\boldsymbol{r}^2 \tag{5}$$

Although somewhat more complicated, this tranformation can be performed to describe a real system of atoms by treating electrons and nuclei seperately and superimposing the contribution of all system bodies:

$$\left[\frac{-\hbar^2}{2m}\sum_{i=1}^{N}\nabla_i^2 + \sum_{i=1}^{N}V(\boldsymbol{r_i}) + \sum_{i=1}^{N}\sum_{j<i}^{N}U(\boldsymbol{r_i},\boldsymbol{r_j})\right]\psi(\boldsymbol{r}) = E\psi(\boldsymbol{r}) \quad (6)$$

where the terms of the Hamiltonian are the kinetic energy of each electron, the interaction energy between each electron and all of the atomic nuclei, and the interaction energy between all of the electrons in the system with each other, respectively [12]. The sums are over all N electrons, with the double sum modified to avoid double counting. While the indexed variable $\boldsymbol{r_i}$ and $\boldsymbol{r_j}$ refer to positions of individual electrons, $\boldsymbol{r}$ is a $3N$-dimensional vector containing the position of every electron; therefore, $\psi(\boldsymbol{r})$ is a many-electron wavefunction, which describes all the electons simulteneously. What rapidly becomes apparent is that the dimensionality of the problem and the coupling between every electron render the equation is analytically unsolvable.

Incidentally, the wavefunction cannot be directly observed. What is measurable through repeated experiment, however, is the probability distribution function (PDF) of a particle's position. Mathematically, this is described by a complex conjugate (expressed as $\psi^*(\boldsymbol{r})$) multiplication with the wavefunction. Another interpretation of this PDF is as an electron density function representing the spatially smeared "electron cloud":

$$n(\boldsymbol{r}) = \psi^*(\boldsymbol{r})\psi(\boldsymbol{r}) \quad (7)$$

In the context of a many-body electron wavefunction, the electron density is calculated by fixing one electron and integrating the many-body PDF over the positions of the other $N-1$ electrons and multiplying by N:

$$n(\boldsymbol{r}) = N\int \mathrm{d}\boldsymbol{r}_2 \ldots \int \mathrm{d}\boldsymbol{r}_N \psi^*(\boldsymbol{r}, \boldsymbol{r}_2, \ldots, \boldsymbol{r}_N)\psi(\boldsymbol{r}, \boldsymbol{r}_2, \ldots, \boldsymbol{r}_N) \quad (8)$$

Note that this density describes the measurable electronic features of an atomic system and is dependent on only on a single 3-component position vector, rather than the 3*N* dimensional wavefunction $\psi(\boldsymbol{r})$ [12]. It is through this electron density that DFT relates to the first-principles description of quantum mechanics.

Hohenberg-Kohn Theorems

The utility of using electron density to describe an atomic system was established via two theorems by Kohn and Hohenberg, and the methodology for determining said electron density was postulated by Kohn and Sham. Both theorems are important for understanding why DFT can be used predictively.

Theorem 1: *The ground-state energy of an electronic system is a unique functional of the ground-state electron density* [2].

Here, a functional is a function that maps a function to a real number. Kohn and Hohenberg showed that the ground-state electron density determines external potential up to an additive constant, the second term in Equation 6. Since this is the only system-dependent term in the Hamiltonian and the Hamiltonian determines the properties of the system, the theorem follows. The implication of this theorem is that the ground-state wave function, which determines the properties of the system, maps directly onto the ground state electron density.

Theorem 2: *The electron density that minimizes the energy of the functional is the true electron density corresponding to the full solution of the Schrodinger equation* [2].

This theorem means that if the lowest-energy configuration can be identified, that electron density is exactly the ground-state electron configuration. This means that variational calculus can be used to minimize the functional.

With these two theorems, we can begin to develop a methodology for determining the ground-state electron density. The energy functional has the following form,

$$E[n] = T[n] + U[n] + \int V(\boldsymbol{r})n(\boldsymbol{r})\mathrm{d}\boldsymbol{r} \tag{9}$$

where *T* and *U* are universal functionals corresponding to kinetic energy and electron-electron interactions and *V* is the system dependent potential from the nuclei.

Kohn-Sham Formulation

These theorems mean that it is possible to get a first-principles description of a material system. However, in order to solve for those terms which can be solved analytically, it is necessary to first have expressions for the universal functionals. This raises the question, "How does one express kinetic energy in terms of electron density?" In order to circumvent this problem, we construct a Kohn-Sham system of *N* non-interacting electrons with a modified potential such that the ground-state electron density is the same as our real system. These non-interacting electrons occupy Kohn-Sham orbitals, $\varphi_i(\boldsymbol{r})$. The electron density can then be written as the following:

$$n(\boldsymbol{r}) = \sum_{i}^{N} |\varphi_i(\boldsymbol{r})|^2 \tag{10}$$

The energy functional is now written as a functional of Kohn-Sham orbitals:

$$\begin{aligned} E[\{\psi_i\}] = -\frac{\hbar^2}{2m}\sum_i \int \psi_i^* \nabla^2 \psi_i \mathrm{d}\boldsymbol{r} + \int V(\boldsymbol{r})n(\boldsymbol{r})\,\mathrm{d}\boldsymbol{r} \\ + \frac{e^2}{2}\iint \frac{n(\boldsymbol{r})n(\boldsymbol{r}')}{|\boldsymbol{r}-\boldsymbol{r}'|}\mathrm{d}\boldsymbol{r}\,\mathrm{d}\boldsymbol{r}' + E_{\mathrm{XC}}[\{\psi_i\}]. \end{aligned} \tag{11}$$

where the first term is the kinetic energy of all electrons in the system, the second is the attractive effect of charge between the electrons and nuclei, the third is the repulsive effect of charge between pairs of electrons, and the last term contains any additional effects not covered by the first four [12]. The first three terms are are single-particle or pair contributions and can expressed analytically. The last term embodies any quantum mechanical effects from exchange and corelation not captured in the other terms.

As mentioned previously, the second Hohenberg-Kohn theorem allows us to use variational methods to minimize this functional. This yields the Schrödinger-like Kohn-Sham equations:

$$\left[-\frac{\hbar^2}{2m}\boldsymbol{\nabla}^2 + V_s(\boldsymbol{r})\right]\varphi_i(\boldsymbol{r}) = \varepsilon_i\varphi_i(\boldsymbol{r}) \tag{12}$$

where the effective potential, V_s, is given by:

$$V_s(\boldsymbol{r}) = V(\boldsymbol{r}) + \int \frac{e^2 n(\boldsymbol{r}')}{|\boldsymbol{r} - \boldsymbol{r}'|}\mathrm{d}\boldsymbol{r}' + V_{\mathrm{XC}}[n(\boldsymbol{r})]. \tag{13}$$

This does, at first glance, seemed circular because the Hamiltonian depends on the orbitals, but if we start with a good guess for what the electron system is actually like, we can perform a self-consistent loop of solving the eigenvalue problem and reevaluating the Hamiltonian to minimize the system energy in conformance with the second of the Hohenberg-Kohn theorems. Briefly, this means that by first defining a trial electron density, the “known” terms in that equation become solvable. By setting a convergence criterion based on the change in energy between two iterations, we can determine whether the system is in its ground state energy. By solving the Kohn-Sham equations, we iterate towards the minimum energy configuration [3].

The Exchange-Correlation Functional

The last loose end for DFT to address is then the non-pair term, the exchange-correlation functional. This sweeps up the rest of the quantum mechanical effects on the electron system undescribed in the other terms. The term comes from the “Exchange” effect of the many particles’ wavefunctions altering to accommodate the Pauli Exclusion principle, and “Correlation” comes from the addition of that effect to the fictitious many-body statistical model we use with DFT. Much work has been spent developing an analytical form for this functional, though its exact form is unknown for almost all real systems. Research has focused on describing a generalizable exchange-correlation functional that accurately reproduces experimentally observed system properties across a wide array of systems.

The first of these general forms was based on a case for which the exchange-correlation functional can be solved precisely: a uniform electron gas. This is a theoretical space in which the electron density is perfectly uniform. In that case, the exchange correlation is analytically solvable for any chosen electron density. Applying this, the exchange-correlation functional for a real system at a given location is then assumed to be equal to that of a uniform electron gas with the same electron density as that locality. This method of choosing the exchange-correlation functional is called the local density approximation (LDA). Though it is a significant approximation, and does not perfectly reproduce observed properties, it does allow DFT equations to be applied [3].

Other efforts to produce a more realistic picture of the exchange-correlation functional, based on models with greater physical information, have also been developed.

One such, the generalized gradient approximation (GGA), not only includes the local density, but also the local gradient in density; it models both the local density and its rate of change. This is intended to apply a more realistic physical description to the exchange-correlation functional.

Many exchange-correlation functionals have been developed, including several different GGA functionals and other types based on different electronic models, though none can precisely recreate all physical properties observed in experiment. In this thesis, the exchange-correlation functional which is used for all calculations is the one developed by Perdew, Burke, and Ernzerhof (PBE) [13], one of the more common in use.

Born-Oppenheimer Approximation for Core Relaxations

The Born-Oppenheimer approximation is used by DFT codes to perform quantum-mechanically-based dynamic relaxation simulations. One of the most important assumptions made in QM theory is that electrons, being far less massive than the nucleus, more rapidly respond to force and energy gradients than do the nuclei. This approximation is exploited in DFT calculations to simplify the many-body subatomic interactions. The ground-state density of a set of electrons can be calculated for fixed nuclei locations, and then the locations of the nuclei updated based on the force felt by each ion based on local gradients of the total energy. This allows DFT to perform optimization algorithms that minimize the total energy of the system and yield ground-state crystal structures [12].

Unit- and Super-cells with Periodic Boundary Conditions

Now, these DFT equations are still massively complex to solve for any system with a realistic number of constitutive atoms. To bring them down to manageable scale,

other methods to simplify our models need to be taken. One such method would be to decrease the number of atoms in the model. For crystalline materials, this makes good sense, since their defining feature is long-range order in its constitutive atomic arrangement. This order can be fully described by a small set of atoms, known as a unit cell. A unit cell is defined by three lattice vectors — $\boldsymbol{a}_1$, $\boldsymbol{a}_2$, and $\boldsymbol{a}_3$ — which describe the shape and size of region which encloses that representative small set of atoms. Periodic repetitions of that unit cell can be iterated into a complete 1-to-1 model of the bulk crystal, though some naturally occurring errors like interstitial atoms and lattice vacancies intrinsic a real material would be omitted in such a description. One of the most important implications of this arises from the fact that electron density for an isolated atom decays to zero quite rapidly with distance: electron density is tightly local for an atom.

In the aggregate case of a pristine crystalline solid, local electron densities in structurally identical areas can therefore also be modeled as identical; the periodic repetition of structural motifs inherent in crystallinity ensures that a structurally identical area will be found within a few bond lengths. This means that we can describe the electron density as a spatially periodic function for crystalline solids, allowing us to construct a faithful quantum-mechanical model of a bulk crystal with just a few tens of atoms. We then apply periodic images of our model to make the function of electron density continuous and consistent with a bulk material at the model boundary (rather than decaying as would occur at a crystal surface): the form of this periodic electron density is discussed in further on.

For non-pristine models, such as one with a local defect like an impurity or vacancy, we use a model comprised of a few iterations of the unit cell: a supercell. This allows the short-range effects of the defect to be incorporated into the model without losing the long-range order of the electron density at the model boundaries. In the parlance of the lattice vectors mentioned previously, these supercells are integer multiples of the unit cell along one or more of the lattice directions — the supercell can be described as $L\boldsymbol{a_1}, M\boldsymbol{a_2}, N\boldsymbol{a_3}$ — where L, M, and N are positive integers, and $\boldsymbol{a}$ are the lattice vectors of the unit cell in real space.

Projector-Augmented Wave Potentials

Another way to reduce the number of unique entities considered in our calculations is to treat valence and "core" electrons around each atom differently. The valence electrons of each atom in a structure are typically the only electrons that are involved in chemically interesting behavior: the core electrons do not participate in much physically interesting phenomena. Incidentally, the core electrons of each atom are also the most computationally burdensome. This is a side-effect of the smaller space that they occupy, as the enforcement of wavefunction orthogonality means that the wavefunction of each electron has much more variance, a shorter wavelength, within the smaller space than does the wavefunction of a valence electron. Fully solving this would necessitate a very spatially high-resolution calculation, but it turns out that solving for a system that freezes the core electrons still gives good results, while also being significantly more computationally efficient. The frozen core technique that is used in our study is called projector augmented-wave (PAW) potentials, which models the core electrons as a frozen cloud of local charge with a modified ionic potential that accounts for these core

electrons. The projector augmented-waves themselves are the basis which accommodates the potentials used to make this simplification [4,12].

Reciprocal Space and *k*-points

Because of the periodic nature of the crystals we wish to study, implementing DFT is significantly easier in reciprocal space. With a periodic crystal lattice, an expedient way to express the electron density wavefunction is with a periodic wavefunction, described by Bloch waves of the form:

$$\psi(\boldsymbol{r}) = \mathrm{e}^{\mathrm{i}\boldsymbol{k}\cdot\mathbf{r}} u(\mathbf{r}) \tag{14}$$

where *u* is a function that periodic function which matches to the periodicity of the crystal system. The exponential term here enables a periodic expression of the wavefunction with its period length circumscribed by the unit cell.

There are some important ramifications for using reciprocal space that are worth being aware of, though the specific construction of reciprocal space is not particularly important to our results. Much as how the crystal structure can be described by a unit cell in real space, the corresponding reciprocal lattice is defined by a reciprocal space unit cell. These reciprocal lattice vectors can be described as function of the real space lattice vectors, like so:

$$\boldsymbol{b}_1 = 2\pi \frac{\boldsymbol{a}_2 \times \boldsymbol{a}_3}{\boldsymbol{a}_1 \cdot (\mathbf{a}_2 \times \boldsymbol{a}_3)}, \quad \boldsymbol{b}_2 = 2\pi \frac{\boldsymbol{a}_3 \times \boldsymbol{a}_1}{\boldsymbol{a_2} \cdot (\mathbf{a}_3 \times \boldsymbol{a}_1)}, \quad \boldsymbol{b}_3 = 2\pi \frac{\boldsymbol{a}_1 \times \boldsymbol{a}_2}{\boldsymbol{a_3} \cdot (\mathbf{a}_1 \times \boldsymbol{a}_2)} \tag{15}$$

The direction of this reciprocal space lattice vector is described by the cross product of two of the real space lattice vectors and its magnitude by the inverse length of the other real space lattice vector. The most important point is that longer real space lattice directions correspond with shorter reciprocal space lattice vectors in the same way that longer wavelengths correspond to shorter wavevectors [12].

Recall from the Hohenberg-Kohn theorems that an important part of DFT calculations is solving integrals which, for the most part, do not have analytical solutions. In computational physics, numerical solutions to such integrals are common and mostly involve rendering the integral as discrete sections rather than a continuous function to approximate a solution. One such rendering would be the trapezoid method. For these numerical methods, the greater the number of discrete sections used in the description, the more accurate the computed result. In DFT, the number of discrete sections used in solving the electron density functional is defined by the user through the number of referenced points in reciprocal space along each reciprocal lattice direction, called *k*-points. As with real space integrals, the convergence of the calculation to an accurate value increases with the number of *k*-points used; increasing the number of *k*-points is referred to as using a finer *k*-point mesh. Once of the idiosyncrasies of reciprocal space, however, is that the longer the lattice vector is in real space, the fewer *k*-points are needed to get a converged computation of an integral along that direction. This is because of the inverse relationship between the length of the reciprocal space vector and the real space vector.

In prior times, even earlier this decade, when DFT calculations were performed singularly and computational resources were scarce enough that minimizing *k*-points while ensuring convergence was a serious consideration, convergence as a function of *k*-point density would be published with results. Nowadays, computational resources are less scare and computers powerful enough to calculate high density *k*-point meshes for most models. Our standard practice is to use a simple rule of thumb for deciding on the *k*-point mesh: we divide 25 by the lattice vector length (measured in Å) in a given

direction, and use the nearest integer as the number of *k*-points in that direction for relaxation calculations. For static calculations, which are our final optimizations, we use a finer mesh which uses thrice as many *k*-points in each direction.

Special Quasi-Random Structures

Another principal method used in this thesis which deserves some explanation is the generation of Special Quasi-Random Structures (SQS), introduced by A. Zunger and associates [14]. This method was proposed in the 1990's as an expedient means for simulating a randomly dispersed alloy in a periodically iterated small supercell comprising mere tens of atoms. Selecting a best guess for a random alloy to study is valuable because an alloy's properties are a function of its configuration, and relatively simple systems have a rapidly divergent number of possible configurations. The example Zunger uses in his paper to illustrate this is a binary compound with N equivalent sites: the number of possible configurations is 2^N [14]. Many crystalline unit cells contain tens of atoms, ballooning to thousands of possible configurations for study. Prior to this method, most alloy calculations had relied on either a single randomly assigned supercell or a small set of randomly assigned supercells. The improvement offered by SQS is that a single cell can model a random alloy based on matching the correlation functions of the atoms in the cell to the correlation function of a long-range random alloy.

The correlation function measures the ensemble average of some physical property over all of the configuration interaction parameters in the cell. In the supercell, each site is given a variable which associates to its species. Then a set of sublattices — known as clusters — is defined within the cell, each containing some number M of atoms

within a user-selected distance of one another. The correlation function is given as the product of the species variables within the sublattice, shown here:

$$\overline{\Pi}_{\alpha}(\boldsymbol{\sigma}) = \frac{1}{N_{\sigma} m_{\alpha}} \Sigma_{\beta \equiv \alpha} \Pi_{i \in \beta} \sigma_i \tag{16}$$

where $\overline{\Pi}_{\alpha}$ is the correlation matrix, $\boldsymbol{\sigma}$ is a distinct configuration, N_{σ} is the number of configurations of that type, α is a symetrically distinct cluster, m_{α} is the multiplicity of cluster α, and β is the set of clusters equivalent to α. Any function of the alloy configuration — properties included — can be written as a weighted sum of multi-site cluster functions.

For a perfectly random cell approaching infinite size, the ensemble average of the correlation functions vanishes to zero. The purpose of the SQS method then is to assign positions in a small *N* atom supercell for which the collection of distinct correlation functions (of each individual cluster) best matches the ensemble average of the perfectly random alloy. Usually, the clusters are defined as only doublets and triplets, which include nearest neighbors and second-nearest neighbors, since this is the length limit of the interactions which govern most material properties. Implementation of the method is a standard Monte Carlo simulation which updates system to converge the distinct correlation functions of the sublattices to the ensemble-averaged ones.

With increasing atom count, the SQS method shows far more rapid convergence of the distinct correlation functions to the ensemble-averaged correlation functions than does a statistically valid set of true random cells. In effect, this shows that SQS are more representative of random alloys than other methods, especially for calculating properties dominated by short-range interactions. The implementation package that we use to create our SQS is the Alloy Theoretic Automated Toolkit (ATAT) [15].

Chapter 3: Bi Doping of β-Ga_2O_3 for Changing the Valence Character and Enabling *P*-Type Conductivity

Introduction

β-Ga_2O_3 is a wide gap (experimentally observed to be 4.9 eV [16]) semiconductor that has garnered much interest as a candidate for next generation power electronic devices. In its bulk form, it is optically transparent on the whole visible spectrum up to 260 nm UV [17] and has a high theoretical breakdown field of 8 MV/cm [18]. Combined, these properties make β-Ga_2O_3 a promising material for functional transparent and high-power electronic devices. With the capacity to be grown in large single crystals by melt-growth techniques, β-Ga_2O_3 is expected to be an economical material for device fabrication [19]. At smaller scales, a wide variety of nanostructures involving β-Ga_2O_3 have been synthesized, indicating that it could be used in any number of novel applications [20, 21]. Functionality at these two length scales make β-Ga_2O_3 promising candidates for a wide range of devices. While native *n*-type conductivity in β-Ga_2O_3 allows it to be used in gas sensors [22] and in normally-on or depletion-mode electronic devices, demonstration of *p*-type conductivity would greatly expand the range of possible applications [23]. *p*-type doping in Ga2O3 would allow the fabrication of *p*-*n* homostructural junctions, enabling fabrication of bipolar junction transistors. Thus far, conclusive and replicable demonstrations of *p*-type doping in Ga_2O_3 remained unrealized.

Many theoretical studies have been devoted to explaining the elusiveness of *p*-type doping in β-Ga_2O_3; one of the reasons *p*-type doping has been difficult is the presence of strong *n*-type behavior caused by unintentional dopants [24, 25]. Other theoretical studies have indicated that the low energy of the valence band maximum

(VBM) relative to the vacuum level is an obstacle to *p*-type conductivity; candidate dopants expected to introduce acceptors tend to form deep-level states that trap charge carriers, rather than shallow-level states that readily exchange carriers with the VBM [26]. Additionally, the large electronegativity of the oxygen atoms — the 2*p* orbitals of which comprise the valence band edge in β-Ga_2O_3 and other wide gap oxide semiconductors — effectively trap holes as localized polarons, limiting their mobility [27, 28]. In order to combat this, Cu has been proposed as a dopant to increase the dispersion of the valence band, reducing the effective mass of the holes, through hybridization of the Cu 3*d* orbitals and O 2*p* orbitals [29]. Our approach is similar in that we seek to alter the valence character, but we propose doing so by doping with Bi: the Bi 6*s* electrons are similar in energy to the O 2*p* electrons and benefit from less localization than the *d*-orbital states proposed with Cu.

Recently, Sabino et al. have shown using DFT calculations that doping with Bi indeed creates mid-gap electron states in the band gap of bixbyite-structure In_2O_3, a close cousin to Ga_2O_3 in terms of valence character [30]. That group has also shown that doping Ga_2O_3 with Bi leads to similar defect states located in the band gap of pristine Ga_2O_3 [31]. These electron states in the intermediate band are natively occupied by the Bi 6*s* electrons, becoming a new valence band. They note that, by itself, this is insufficient to achieve *p*-type conductivity; intermediate states need to be shallower and empty to enable *p*-type conduction. Via Density Functional Theory (DFT) calculations, we determine that Bi can likely be introduced at dopant concentrations by comparing energetics with respect to the end members Ga_2O_3 and Bi_2O_3 that form the convex hull. We confirm that introduction of Bi, even at dopant levels, in Ga_2O_3 causes the formation

of an intermediate band in the band gap of pristine Ga_2O_3, which is comprised of the Bi 6*s* electrons. In our work, we explore the charge transitions and traps of the Bi dopant as they compare to those of the native defects and confirm the need for additional dopants to achieve *p*-type conduction. Identification of the trap states of Bi defects verifies that the Bi intermediate bands are occupied. The associated charge transitions for the intermediate states are found to occur at a high energy cost compared with native defects, indicating a robust change in the valence character. The intermediate bands introduced by Bi change the level and orbital character of the valence band edge, potentially transforming otherwise deep, co-dopant acceptors into shallow ones through the elevated level and increasing the mobility of charge carriers through the delocalized *s*-orbital character.

Methods

All results are based on DFT calculations performed with the Vienna Ab-initio Simulation Package (VASP) [4], using the projector augmented-wave (PAW) potentials [5] with the Perdew, Burke, and Ernzerhof (PBE) [13] exchange-correlation functional. We include the 3*d* electrons as valence electrons for Ga. It has been shown that exclusion of the 3*d* electrons in DFT simulation incorrectly favors the α-Ga_2O_3 corundum phase to be the ground state, rather than the experimentally verified β-Ga_2O_3 monoclinic phase [32]. Similarly, we include the 5*d* electrons in the valence for Bi. Geometric relaxations were performed with a Γ-centered *k*-points mesh such that the mesh size multiplied by cell size roughly equated to 25 in each direction for relaxations, and 75 for spin-orbit coupled static calculations. Convergence criteria was set at 1E-6 eV for self-consistent electronic optimization, and 5E-3 eV/Å for ionic relaxations. Unrelaxed, undoped structures were taken from the Materials Project database [33]. The alloy-concentration

structures were generated using the special quasi-random structures (SQS) method [14] as implemented by the Alloy Theoretic Automated Toolkit (ATAT) software package [15], taking care to constrain species distributions to the thermodynamically favored lattice sites by explicitly noting which atomic species could occupy each site in the ATAT settings. The visualizations were created using the VESTA (Visualization for Electronic and Structural Analysis) software [34]. To correct for the unphysical, short-range electrostatic interactions between charged atoms and their periodic images, we employ the screening method introduced by Freysoldt et. al [35].

Results and Discussion

We first consider energetics of Bi atom incorporation into the β-Ga_2O_3 lattice. β-Ga_2O_3 has a monoclinic structure, space group $C2/m$, with five unique lattice sites: two Ga sites and three O sites. The structure is shown in **Figure 3.1(a)** With a diverse set of lattice locations, it is important to establish whether one site is preferred for a foreign dopant, Bi in this case, in an alloy or doped material. This allows simulated replacements to be informed by thermodynamic likelihood rather than random selection. The two types of Ga sites are tetrahedrally coordinated Ga1 and octahedrally coordinated Ga2. These sites are shown in **Figure 3.1(a)** in light green and dark green, respectively. There are two O sites that are 3-coordinate (O1 and O2) and one tetrahedral coordinate (O3). The 3-coordinate O sites are identified by their adjacent Ga polyhedrons: O1 is bound to two Ga2 sites and one Ga1 site, while O2 is bound to one Ga2 site and two Ga1 sites. For each of these five unique sites, the enthalpy of a Bi substitution was calculated to determine site favorability. In the case of the Ga sites, a simple replacement was used. For the O sites, we used an anti-site pair (ASP) to maintain charge neutrality. In practice,

this meant that when an O site was selected to be occupied by Bi, an adjacent Ga atom was replaced with an O atom. During geometric optimization, the Bi and O atoms corresponding to the ASP returned to their preferred cation and anion sites, respectively, indicating that the ASP configuration was not a local energy minimum. Of the two Ga sites, the octahedral site proved more favorable for Bi occupancy by 52 meV/cation. Other works have used 79 meV/cation energetic favorability to justify preferential site occupancy up to 50% alloy concentration [36]. Our work uses a maximum of 33 % Bi alloy concentration; we believe this lower site bias justifies preferential site occupancy for the lower concentration. Characterization of the electronic structure of the doped compound was therefore undertaken with Bi occupying the Ga2 site, shown in the darker green in **Figure 3.1(a)**. This addressed the question of where in the unit cell of β-Ga_2O_3 a Bi dopant might localize.

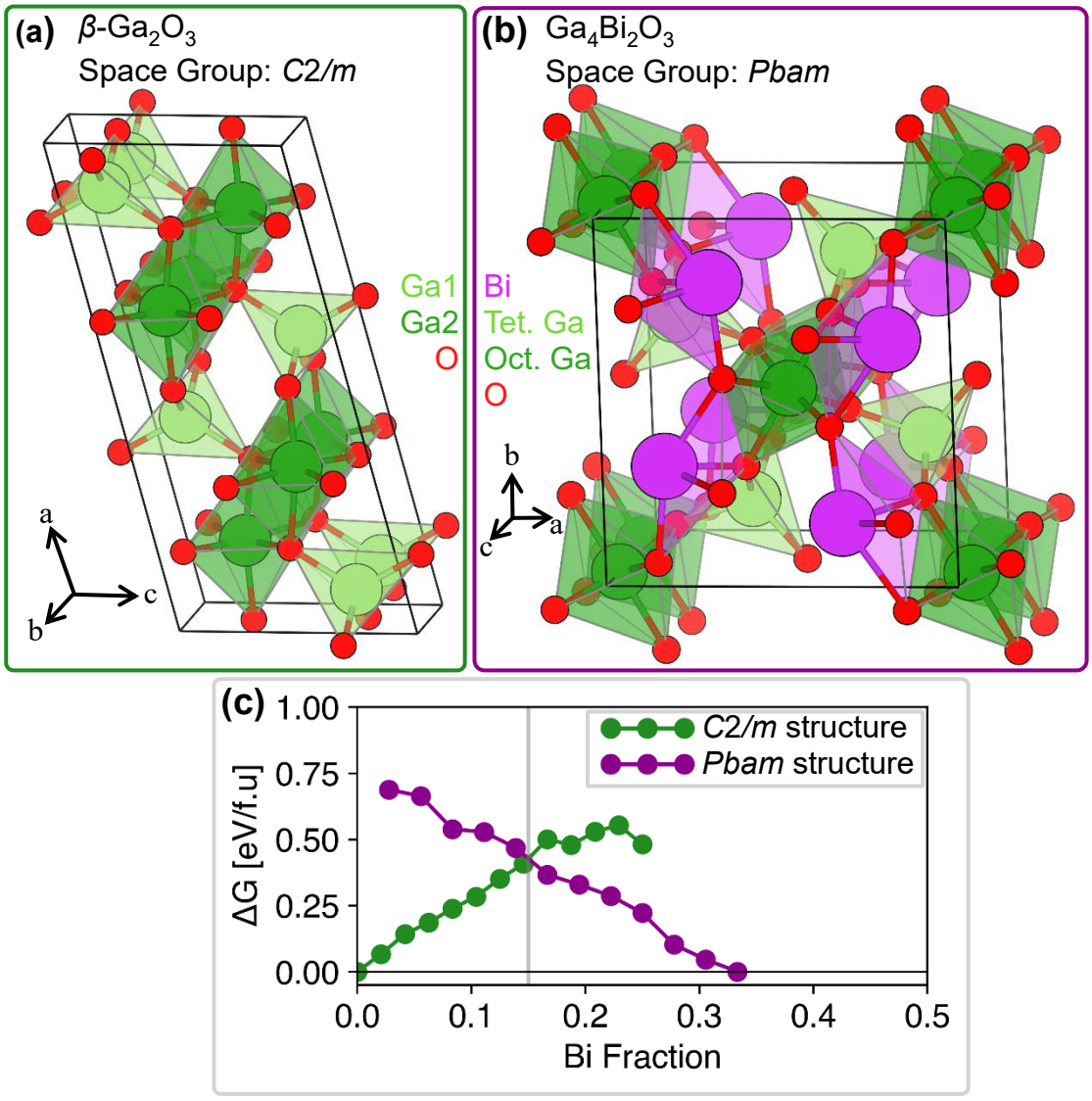

Figure 3.1: (a) The unit cell of β-Ga_2O_3, emphasizing the unique Ga sites with light green for the tetrahedral coordination with oxygen (red) and dark green for the octahedral. (b) The *Pbam*-structure $Ga_4Bi_2O_9$ unit cell, with the same emphasis on different Ga sites. The Ga atoms take the same two coordinations as in the β-Ga_2O_3 structure, with small distortions on the octahedral sites. Bi atoms are in purple. (c) The Gibbs free energy of the two structures relative to the endmembers at 298K, matched to

the box colors of (a) and (b). The lines connecting calculated energies are to guide the eye.

The feasibility of alloying Bi into β-Ga_2O_3 is determined by the miscibility of the mixture. Crucially, we needed to confirm that an alloy with Bi would not stabilize an alternative structural phase over the monoclinic structure of β-Ga_2O_3. For a competing phase, we found that there was one ordered compound on the convex hull of Ga and Bi oxides at the Materials Project database, with stoichiometry $Ga_4Bi_2O_9$ [33]. The structure of this material is in the orthorhombic *Pbam* space group*;* its unit cell is pictured in **Figure 3.1(b)**. The β-Ga_2O_3 monoclinic structural phase is referred to hereafter as the β-structure, to contrast with the *Pbam* space group designation of the $Ga_4Bi_2O_9$ compound. Using lattice site replacements, we explored the range of (total) cation concentrations between 0% and 33% Bi—the Ga/Bi cation ratio in $Ga_4Bi_2O_9$—on both the β- and *Pbam*-structures. For the β-structure, we used the SQS method to replace Ga atoms with Bi on the favored Ga2 octahedral site; for the *Pbam*-structure, we used the SQS method to replace Bi atoms with Ga on the 5-coordinate Bi sites. Subsequent DFT calculations allowed the lattice parameters and atomic coordinates to relax, consistent with the alleviation of internal stresses of alloy concentrations of the introduced species. Inclusion of a temperature-dependent structural entropy term for these disordered alloys allowed quantification of the free energy of the structure and direct comparison of their energies; by scaling the entropic contribution with temperature, we hoped that we could identify a compositional region of stability. The contribution of this term is ultimately negligible compared to the formation enthalpy at the relatively large Bi concentrations that we studied, but it can stabilize low-concentration mixtures. For Bi concentrations of less than

about 15%, we observe that the Gibb's free energy of the alloy at room temperature is lower in the *β*-structure than in the *Pbam*-structure. A plot of these results is shown in **Figure 3.1(c)**. We conclude that the *β*-structure is therefore likely to be the dominant crystal configuration at low Bi concentrations. However, because there is no concentration of Bi for which the free energy is below zero relative to the end members, any solid solution of Bi in *β*-Ga_2O_3 will be at best metastable. We note that metastability is not necessarily such a bad thing for a material; glasses, which are ubiquitous materials in the modern world, are metastable materials. No alloy composition was found to be stabilized with the structural entropy contribution for any temperature less than the melting temperature of pristine *β*-Ga_2O_3. To encourage formation of a metastable solid solution, we focus on including low concentrations of Bi rather than alloying at high concentration with both Bi and Ga as principle elements.

The electronic behavior of the uncharged, Bi-doped structure was explored using DFT with the PBE exchange-correlation functional with spin-orbit coupling (SOC). In contrast with the method used above to establish miscibility, these calculations fixed the lattice parameters: simulating the local stress imparted by a diffuse dopant in a bulk material. We found that at low concentrations of Bi, occupied intermediate states were introduced in the intrinsic band gap of *β*-Ga_2O_3, reflected by the density of states in **Figure 3.2(a)**. By projecting the density of states onto an atomic orbital basis, we determined that the intermediate states are dominated by the Bi 6*s* states as shown in **Figure 3.2(b)**. This indicates that the 6*s* electrons are of an appropriate energy level to be used for altering the valence bands. The remainder of the intermediate bands were dispersed across all of the O atoms in the supercell, rather than being localized to the O

near to the defect. This is shown in a plot of the partial charge density shown in **Figure 3.2(c)**. These calculations assumed uncharged defects; the available charge states of the intermediate band were also explored to determine if they are low-energy trap states.

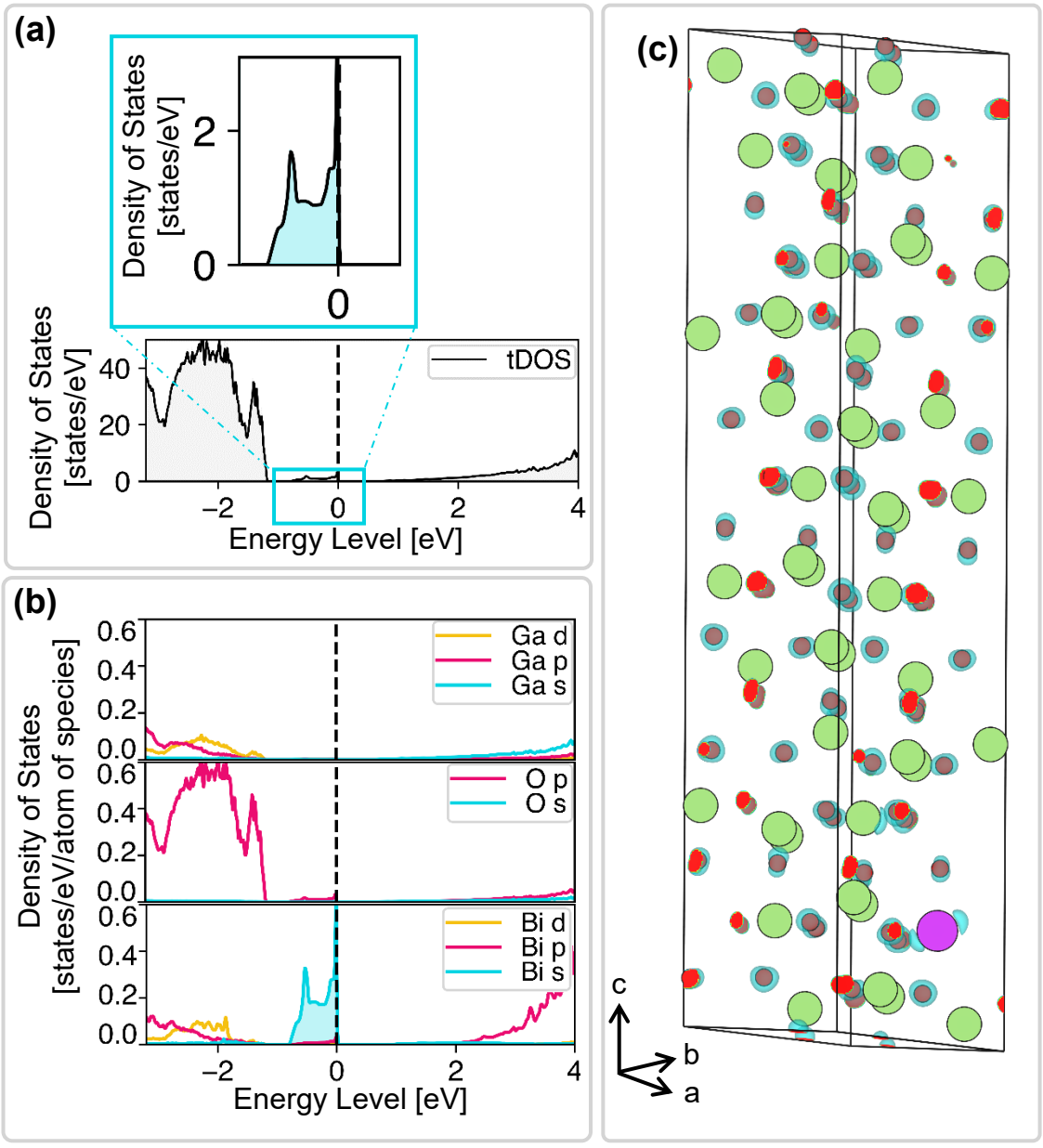

Figure 3.2: (a) The total density of states for a 1/48 cation concentration Bi dopant. The fermi level is taken to be the edge of the intermediate band. The intermediate states

(in blue) are blown up for emphasis. This calculated DOS includes SOC, which we observe results a broadening of the intermediate band. (b) the projected density of states for each atomic species onto the atomic orbital basis. Note that these partial densities are normalized to a per-atom contribution. The primary contribution to the mid-gap states derives from the Bi *s*-orbitals, with an additional contribution from the O *p*-orbitals. (c) Visualization of the partial charge density (light blue) of a 120-atom supercell for the energy range of –1 to 0 that covers the only the intermediate states. All Ga atoms are in light green to reduce the number of colors in the figure and draw attention to the light blue charge density isosurfaces.

The formation energy of a charged defect as a function of the Fermi level was calculated using the formulation of Freysoldt et al [35], which includes corrections for the Fermi level, long- and short- range potential effects, and an alignment term to reference to the bulk. Changing the charge of defect states can be done by explicitly adding or removing electrons from the system. By plotting the formation energies of these charged defects as a function of Fermi level, we can determine the energy levels of trap states based on intersections corresponding to charge transitions. In some cases, this method did not show a clear extreme of the local potential between the point charge in the supercell and its periodic image. In these cases, we assumed that the charge was delocalized, and did not apply a correction. Shallow trap states, the types that we hope to observe, are states close to the band edges (valence or conduction band) from where charge carriers can be excited between the bands and traps by thermal vibrations. In aggregate, these carriers can exchange with the valence band, which is the essence of *p*-type conduction.

We applied this method to the Bi dopant and to vacancies on each native site. Native defects are unavoidable artifacts of synthesis; as a result, the natural vacancies and dopant defects will present competing traps for any free charge carriers. Concentration of these native vacancies can be controlled by changing the synthesis atmosphere but cannot be wholly eliminated. For the Bi-rich chemical potential condition, we find that the formation energy of a positively charged O vacancy is between 2.87 and 3.45 eV (depending on the O site) lower than the formation energy for a positively charged Bi point defect, as show in **Figure 3.3(a)**. This is in good agreement with the both the energy level of the O vacancy traps and the formation energies of the defect states calculated by Zacherle et. al [25]. These positively charged O vacancies transition between 2+ and neutral: it has been previously shown that the V_O 1+ charge state is unstable for all sites in β-Ga_2O_3 [37]. Notably, it has been shown that native charged vacancies are unlikely to occur in high concentrations in most materials [38]. We find that the (0/+) transition levels of the Bi charge defects are contained within the intermediate band, shown in **Figure 3.3(b)**; this indicates that the 6*s* orbitals are electronically active. Critically, the (0/−) charge transitions of the Bi dopant occur deep in the conduction band, confirming that the intermediate states are fully occupied and not applicable as acceptor trap states.

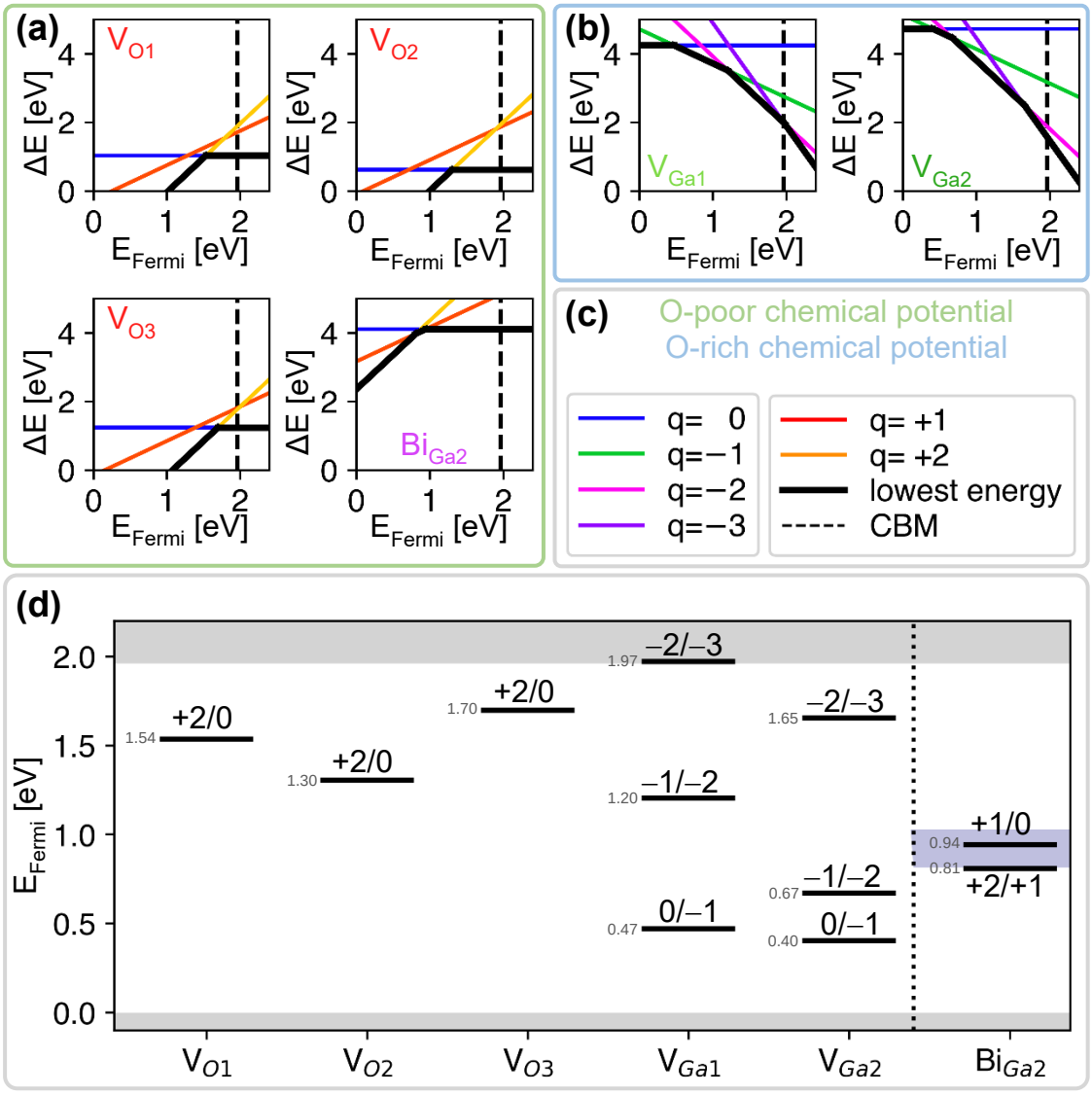

Figure 3.3: (a) Fermi energy of the charge state transitions for native oxygen vacancies and the Bi dopant calculated for an O-poor condition. (b) Fermi energy of the charge state transitions of the native Ga vacancies calculated for an O-rich (Ga-poor) condition. (c) legend for panels (a) and (b). (d) charge transitions, normalized to the intrinsic VBM, of the native vacancies and the Bi dopant. The large numbers indicate the charge transition, and the small numbers report the E_{Fermi} level of the trap state.

Note that these calculations exclude SOC, which results in a narrower intermediate gap.

The lower ΔE associated with charge transitions of the native O vacancy would inhibit charge transitions in the Bi defect states, compensating for any free holes. The reason for this is that the comparatively low energy barrier to the 2+ charge state would encourage localization of holes to those trap states, rather than to the Bi 6*s* states, where the formation enthalpy is higher. The low level of the negative charge states of the Ga vacancies are a good sign for introduction of free holes in the intermediate band, as the preferred charge state of those defects would encourage the transfer of electrons from the Bi impurity to the Ga vacancy trap state, emptying the Bi-derived intermediate bands. The charge transitions that we are most interested in are a carrier exchange between the 0/−1 and −1/−2 V_{Ga} and the Bi_{Ga2} states. Encouraging the formation of these native defects would necessitate extreme care in fabrication, relying on high oxygen chemical potential. This would have the added effect of lowering the concentration of oxygen vacancies, which would take positively charged carriers from the intermediate band. Other possible doping strategies can be considered with the heightened valence band: computational studies have previously reported that Mg and N form deep self-trapped holes rather than free hole carriers [27, 39], but the higher valence band may enable effective codoping with those elements.

Conclusion

To summarize, we compared the Gibb's free energy of a low-concentration Bi-doped β-Ga_2O_3 crystal and determined that it was unlikely to relax into a convex hull structure. Low Bi dopant concentrations seem to be the only available occupancy in the

β-Ga_2O_3 structural phase, due to the high free energy of all computed mixture concentrations. The Bi dopant introduces intermediate defect states in the band gap. These states are filled, and the high formation energy of the (0/+) charge transitions indicates that these represent a substantive alteration of the valence character rather than an introduction of deep-level trap states. The intermediate band, higher in energy than the native valence band edge and more dispersive, could be used to facilitate *p*-type doping, but the Bi dopant, by itself, is unlikely to result in free acceptor states. The higher level of the VBM would allow codopants to form shallow level states rather than the deep level states that acceptor-type dopants had been relegated to previously.

Chapter 4: Pursuit of Improved Thermal Conduction in β-Ga_2O_3 by Alloying with B

Introduction

β-Ga_2O_3 is a wide gap semiconductor which shows promise for high-power and high-frequency electronic applications due to its high breakdown field [40]. The breakdown field has been experimentally measured as 4 MV/cm and theorized to be as high as 8 MV/cm [18]. It is readily dopable *n*-type, with a tunable carrier concentration from the order of 10^{16} to over 10^{20} e^{-}/cm^{-3} [41]. However, the development of devices has been hindered by the poor thermal properties of β-Ga_2O_3, which cause heat retention that negatively impacts device functionality. The thermal conductivity is highly anisotropic with crystallographic direction, measured to be between 11.0 and 26.8 [42] or calculated to be between 16.1 and 21.5 W/m K [43]. Improving the thermal properties without sacrificing the wide band gap could enable highly durable high-power and high-frequency electronic devices based on β-Ga_2O_3.

In semiconductors, the principal carrier of thermal energy is lattice phonons, contrasting with metals, where electrons carry more of the heat energy. As a consequence, the crystal lattice structure of a semiconductor plays a significant role in the thermal properties. Coupled with this is the fact that lattice phonons can scatter electronic charge carriers, reducing the electrical conductivity of the semiconductor. Increasing the thermal conductivity of β-Ga_2O_3 to mitigate some of the electron scattering in high power operation would increase the quality of β-Ga_2O_3 high-power devices. Some improvement in the thermal properties of β-Ga_2O_3 could be possible with a β-Ga_2O_3 phase $GaAlO_3$ alloy: in a recent paper, Mu *et. al* reported using first-principles calculations an improvement of 70-100% (to ~25 W/m K) [44] in the thermal conductivity of $GaAlO_3$

alloy over the unalloyed β-Ga_2O_3 (~15 W/m K) [42]. This is a substantial step, though the thermal conductivity is still lower than that of other modern wide band gap semiconductors such as GaN (110 W/m K) and SiC (700 W/m K) [45]. Further increases in the thermal conductivity would provide a means to operate β-Ga_2O_3 devices at high power and frequency—the applications for which it shows the most promise—without sacrificing the carrier conduction.

The four basic rules which describe the potential for high thermal conductivity in a material, described by G. A. Slack, are 1) low atomic mass, 2) strong interatomic bonding, 3) simple crystal structure, and 4) low anharmonicity [46]. In preserving the other properties and structure of β-Ga_2O_3, we opt to focus on the first two rules as our guiding principles for designing the material. Introduction of the lighter cation Al was the mechanism for improving the thermal conduction in the paper previously referenced. We are interested in alloying with the even lighter Group-13 element, Boron, in an attempt to capitalize on this improvement. B has substantially smaller Shannon ionic radius (0.11 Å in 4-coordinate or 0.27 Å in 6-coordinate) than Ga (0.47Å in 4-cordinate and 0.62Å in 6-coordinate) [47] and prefers 3-cooridnate to the native 4- and 6-coordinations of the cations in β-Ga_2O_3. To counteract these effects, we have also explored the possibility of co-alloying with other Group-13 elements Al and In to try to stabilize the B-containing alloy. Our approach in alloying these elements explores the possibility of high-entropy alloy (HEA) stabilization and a variety of ordered structures to ascertain the stability of B-containing alloys with β-Ga_2O_3. We find that the energy barrier to B alloying in β-Ga_2O_3 is very high and unlikely to be feasible experimentally.

Methods

We use density functional theory calculations [2,3] to explore the energetics and likely formations of the Group-13-oxide alloys. Calculations were performed using the Vienna *Ab-initio* Simulation Package (VASP) [4], applying the projector-augmented wave (PAW) potentials method [5] and the exchange-correlation functional of Perdew, Burke, and Ernzerhof [13]. The inclusion of the outer *d*-orbital electrons in the valence shell of Group-13 atoms has been previously shown to be of critical importance in reporting the experimental ground state of their oxides [32], so we take care to select the appropriate pseudopotential that these electrons are included in the valence of In and Ga for all of our simulations. We use a Γ-centered *k*-points mesh such that mesh size multiplied by cell size roughly equated to 25 in each direction for relaxations, and 75 for static calculations to get a finer simulation mesh for calculation of ground state energies. Our convergence criteria were set at 1E-6eV for electronic optimizations and 5E-3 eV/Å for ionic relaxations. The unrelaxed bulk phases were taken from the Materials Project database [33], and information on probable phases based on the convex hulls of Group-13 oxides reported there. Random alloys were simulated using the special quasi-random structures method [14] as implemented by the Alloy Theoretic Automated Toolkit (ATAT) package [15]. Visualizations of the unit- and super-cells were created using the Visualization for Electronic and Structural Analysis (VESTA) software [34].

Results and Discussion

To help identify the lowest-energy alloy configurations for our alloys, we first relaxed a small supercell with a single cation replacement for B, Al, and In on the two unique cation sites in β-Ga_2O_3. This allowed us to establish site favorability through

comparing the formation enthalpy of the two replacements; these energies are depicted in **Figure 4.1(a)**. We used a 40-atom supercell to calculate the site replacement enthalpies and fixed the lattice parameters to be those of pristine β-Ga_2O_3 in order to simulate the local stresses induced by a diffuse dopant. The formation enthalpies of these site replacements were calculated simply using this formula:

$$\Delta h_{alloy} = \mathrm{E}_{alloy} - \frac{1}{16}\mathrm{E}_{M_2\mathrm{O}_3} - \frac{15}{16}\mathrm{E}_{\mathrm{Ga_2O_3}} \tag{17}$$

where each energy is the VASP-reported total energy of the structure, the fractions represent the cation concentrations, and the *M*-containing oxide energy is the energy of the other species' native oxide: B_2O_3, Al_2O_3, or In_2O_3 (shown in **Figure 4.1(b), (c),** and **(d)**, respectively). We find that both Al and In prefer the octahedral cation site, while B prefers the tetrahedral cation site. Al has the lowest barrier to occupation on either site: we take this to mean that Al will natively occupy octahedral sites; but can occupy tetrahedral sites at a relatively low energetic cost if there are no octahedral sites available. In prefers the octahedral site by such a large margin that we assume all In diffused into β-Ga_2O_3 will take an octahedral replacement site. B shows a significant energy barrier to either site, at 57.5meV/cation on the tetrahedral site and nearly twice that on the octahedral site.

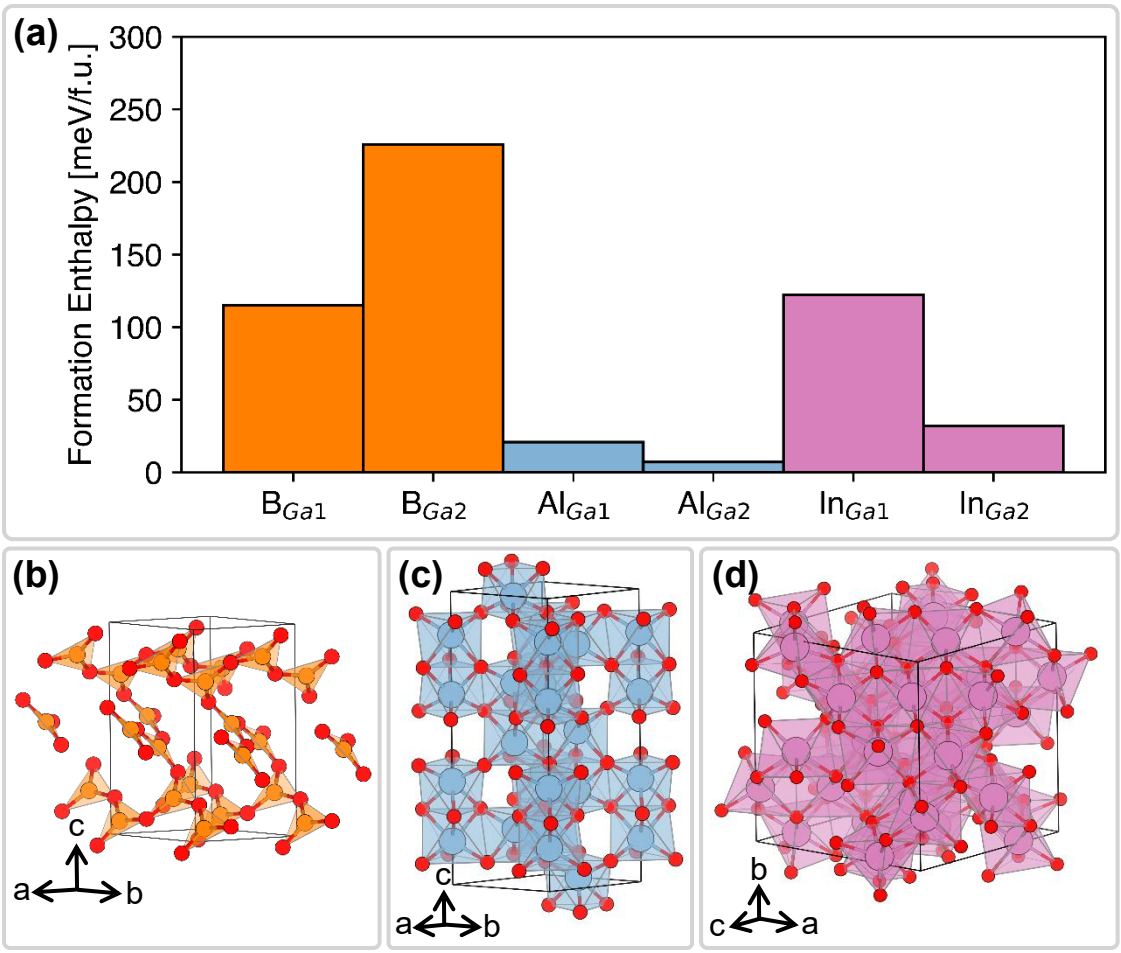

Figure 4.1: (a) Formation enthalpies of site replacements of the Group-13 cations on the non-equivalent cation sites in β-Ga2O3. (b) B_2O_3 used as a reference state for the calculation of formation enthalpy. B atoms are in orange, O atoms are in red. (c) Al_2O_3 used as a reference state for the calculation of formation enthalpy. Al atoms are in blue. (d) In_2O_3 used as a reference state for the calculation of formation enthalpy. In atoms are in purple.

The best-case scenario for an alloy would be one which incorporates a large atomic % of B, to significantly lower the mean atomic mass, and which balances B with In to retain the band gap of pristine β-Ga_2O_3. To explore the possibilities of a high-concentration alloy, we calculated the formation enthalpies of random, shown in **Figure**

4.2(a), and site-preferred equimolar ternary alloys and of ordered binary alloys, shown in **Figure 4.2(b)**. The equimolar alloys calculated were 60 atom cells formed using the ATAT package to create SQS, with the formation enthalpy reference states once again being the cations' native oxides. In the equimolar alloys, the structure formation enthalpy is dramatically reduced by enforcing site preference in the generation of the SQS, shown by the thinner bars for select alloys in **Figure 4.2(a)**. We find that relatively low formation enthalpies can be achieved in the ternary alloy with Ga, Al, and In in equal concentrations, and that the lowest-energy B-containing alloy is the $(B_{1/3}Ga_{1/3}In_{1/3})_2O_3$ compound. **Figure 4.2(b)** depicts the calculated formation enthalpies, once again referenced to the native oxides depicted in **Figure 4.1(b)-(d)**, of equimolar binary ordered alloys for each element with total occupation of the tetrahedral cation sites (thin bar) and octahedral cation sites (thick bar). The octahedral occupied alloys were found to be stable (negative formation enthalpy) for both $GaAlO_3$ and $GaInO_3$. The B ordered alloys were found to have high formation enthalpy, indicating a low chance of formation.

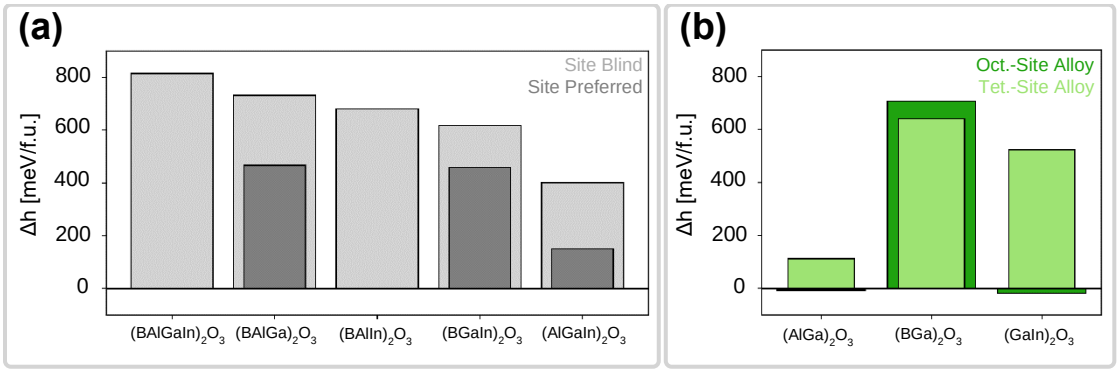

Figure 4.2: Formation enthalpies of quaternary and ternary Group-13-cation alloys with (a) cation disorder and (b) cation ordering.

So why do the B-containing alloys seem to be so unlikely to form? The coordination of B in its native oxide provides a clue: B only takes a planar triangular

coordination with oxygen in its own oxide structure, depicted in **Figure 4.1(b)**. This contrasts with the polyhedral coordinations of the Ga atoms in β-Ga_2O_3, and with the octahedral coordinations of the Al and In oxides. We observed that our *ab-initio* relaxations favored a flattening of the B bonding arrangement into a similar triangular coordination, shown in the **Figure 4.3(b)**. An important barrier to the formation of these ordered alloys was the presence of an equal-cation compound just 4 meV above the convex hull of the Ga and B oxides [33]; a $GaBO_3$ compound with a $R\bar{3}C$ space group, depicted in **Figure 4.3(c)**. This compound, a low-energy structure with the same equimolar ratio as our site-ordered alloys, offers a decomposition target for the high-energy ordered site alloys. We conclude that an alloy with equimolar cation concentration is likely to relax to that phase A key feature of this $GaBO_3$ structure is that there too, B takes a flat triangular coordination. We can glean from the B_2O_3 and $GaBO_3$ structures, and the flattening of the coordination in the DFT relaxations, that B rejects polyhedral coordinations with oxygen, rendering it unlikely that it can be included in a β-Ga_2O_3 alloy.

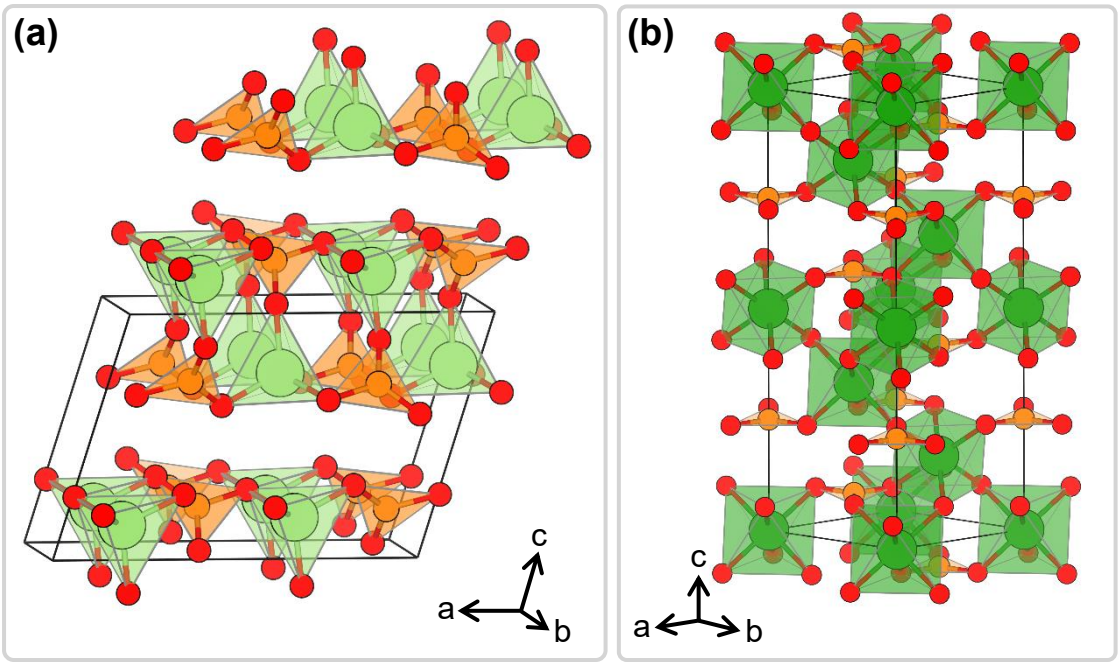

Figure 4.3: (a) DFT-optimized structure of ordered $GaBO_3$ starting from the β-Ga_2O_3 structure with B atoms substituting the octahedral Ga sites. The Ga atoms (light green) are tetrahedrally coordinated with O. (b) $GaBO_3$, a compound found just above the convex hull of B_2O_3 and Ga_2O_3, as reported on Materials Project [33]. The octahedrally coordinated Ga atoms are colored in dark green to differentiate coordination from the tetrahedrally coordinated Ga atoms.

Conclusion

We find that the natural planar triangle coordination preference of B greatly impedes the solubility of B in β-Ga_2O_3.The enthalpic cost of including any concentration of B atoms in the alloy was found to be greater than is likely to be overcome with entropy. Creative orderings were found to lower the formation enthalpy, but not sufficiently to stabilize the alloy. Additionally, the presence of a $GaBO_3$ structure on the convex hull of the B and Ga oxides inhibits an equimolar alloy with B from retaining the β-phase. As a result, high alloy concentrations of B, which would have the best chance of

increasing thermal conductivity of β-Ga_2O_3, would instead decompose into the alternate phase. The thermal conductivity of $GaBO_3$ remain to be explored.

Chapter 5: Conclusions and Outlook

In the preceding chapters, we discussed some of the weaknesses of β-Ga_2O_3 and how they might be addressed. Our exploration focused on the two biggest obstacles which face of β-Ga_2O_3, its lack of *p*-type dopants and its poor thermal properties. Each of these has implications for of β-Ga_2O_3 devices: *p*-type doping would enable bipolar power devices and better thermal properties would enable better performance in high-power devices.

On the issue of *p*-type doping, we used first-principles DFT calculations to explore the changing valence character of β-Ga_2O_3 through inclusion of Bi at low concentrations. Our calculations indicate that the Bi 6*s* electrons form an intermediate band above the valence band of the pristine material, which could enable otherwise deep acceptors to act as *p*-type dopants. The next step will be for experimentalists to establish concrete solubility limits for Bi — the number of atoms required to perform DFT calculations on lower concentrations of Bi is too large for current computing resources to handle. If a stabilized alloy concentration can be identified, then the next step will be to prototype devices to verify whether *p*-type conduction can occur. This is non-trivial, as testing carrier type requires Hall Effect measurements.

Further first-principles calculations in this space could help identify useful codopants against the intermediate band. Many of the electron-deficient species (compared to the native Ga or O) had previously been written off as *p*-type dopants, since their trap levels were calculated to be too deep. This elevated intermediate band could enable effective charge transfer to those deep level dopants. Additionally, hybrid functionals could be employed to accurately compute the band gap, and then locate the

energy levels of the trap states in the band gap. This would allow accurate computation of the trap state levels with respect to the intermediate band and give a better picture of which codopants would be most promising. In a side project, we anecdotally observed that Sb, with the same group as Bi, also introduced an intermediate band. An exploration of the solubility of Sb in β-Ga_2O_3 was not conducted, but that alloy could prove more easily stabilized than the Bi alloy we studied. Further calculations with more devoted interest would also allow comparison between these two intermediate bands, and potentially offer a second intermediate level that could be explored against useful trap states.

In Chapter 4, our calculations indicated that B was unlikely to form a miscible alloy with Ga_2O_3, and that sufficient improvement in the thermal properties of β-Ga_2O_3 through alloying Group-13 elements is unlikely outside of Al. Other methods, beyond those we explored in our study, might be explored to improve the thermal properties of the material. Our study was confined to the Group-13 elements, and much of the intuition we gained in forming our conclusions was coupled with on the preferred coordination of the cations in their native compounds. Based on that, we could expand the design space include other light metals which more readily accept the tetrahedral and octahedral arrangements of the cations in the β-Ga_2O_3 structure.

Calculations on other compounds with similar structures to β-Ga_2O_3 also offer some clue as to an effective strategy for improving thermal conductivity. Most of the materials with similar structures reported on the Materials Project database were oxides, but there were also some fluorides, which could have a different response to the alloying techniques we used. The $GaBO_3$ structure on the convex hull is also intriguing as a more

thermally conductive compound, as its structure has a) lower mean atomic mass than β-Ga_2O_3 and b) a more symmetrical unit cell.

References

[1] Callister, W.D. and Rethwisch, D. G (2014). *Material Science and Engineering: An Introduction* (9th Edition) (pp. 739). John Wiley & Sons, Inc.

[2] Hohenberg, P. and Kohn, W. (1964). Inhomogeneous Electron Gas. *Physical Review 136(3B)*. doi:10.1103/PhysRev.136.B864.

[3] Kohn, W. and Sham, L. J. (1965). Self-Consistent Equations Including Exchange and Correlation Effects. *Physical Review 140(4A)*. doi:10.1103/PhysRev.140.A1133.

[4] Kresse, G. and Furthmüller, J. (1996). Efficient Iterative Schemes for *Ab-Initio* Total-Energy Calculations Using a Plane-Wave Basis Set. *Physical Review B 54*. doi:10.1103/PhysRevB.54.11169.

[5] Kresse, G. and Joubert, D. (1999). From Ultrasoft Pseudopotentials to the Projector Augmented-Wave Method. *Physical Review B 59*. doi:10.1103/PhysRevB.59.1758.

[6] Davisson, C. and Kunsman, C. H. (1923). The Scattering of Low Speed Electrons by Platinum and Magnesium. *Physical Review 22*. doi:10.1103/PhysRev.22.242.

[7] Davisson, C. and Germer, L. H. (1927). The Scattering of Electrons by a Single Crystal of Nickel.

[8] Thomson, G. P. (1928). Experiments on the Diffraction of Cathode Rays. *Proceedings of the Royal Society A*. doi:10.1098/rspa.1928.0022.

[9] Sturm, S., Köhler, F., Zatorski, A., Wagner, A., Harman, Z., Werth, G., Quint, W., Keitel, C. H., and Blaum, K. (2014). High-Precision Measurement of the Atomic Mass of the Electron. *Nature 506 (467-470)*. doi:10.1038/nature13026.

[10] de Broglie, L. (1924). Recherches sur la Théorie des Quanta (Researches on the Quantum Theory). Thesis (Paris).

[11] Schrödinger, E. (1926). Quantisierung als Eigenwertproblem (Quantization as an Eigenvalue Problem). *Annalen der Physik 384(4)*. doi:10.1002/andp.19263840404.

[12] Sholl, D. and Steckel, J. A., (2009). *Density Functional Theory: A Practical Introduction*. John Wiley & Sons, Inc.

[13] Perdew, J. P., Burke, K., and Ernzerhof, M. (1997). Generalized Gradient Approximation Made Simple. *Physical Review Letters 77*. doi:10.1103/PhysRevLett.77.3865.

[14] Zunger, A., Wei, S. H., Ferreira, L. G., and Bernard, J. E. (1990). Special Quasirandom Structures. *Physical Review Letters 65*. doi:10.1103/PhysRevLett.65.353.

[15] van de Walle, A., Tiwary, P., de Jong, M., Olmsted, D. L., Asta, M., Dick, A., Shin, D., Wang, Y., Chen, L. Q., and Liu, Z. K. (2013). Efficient Stochastic Generation of Special Quasirandom Structures. *Calphad 42*. doi:10.1016/j.calphad.2013.06.006.

[16] Zhang, Y., Yan, J., Li, Q., Qu, C., Zhang, L., and Li, T. (2011). Structure and Optical Properties of N-Doped β-Ga_2O_3 Films Deposited by RF Magnetron Sputtering. *Physica B: Condensed Matter 406*. doi:10.1016/j.physb.2011.05.011.

[17] Stepanov, S. I., Nikolaev, V. I., Bougrov, V. E., and Romanov, A. E. (2016). Gallium Oxide: Properties and Applications – a Review. *Reviews on Advanced Materials Science 44*.

[18] Higashiwaki M., Sasaki K., Kuramata A., Masui T., and Yamakoshi S. (2012). Gallium Oxide (Ga_2O_3) Metal-Semiconductor Field-Effect Transistors on Sing-Crystal *β*-Ga_2O_3 (010) Substrates. *Applied Physics Letters 100*. doi:10.1063/1.3674287.

[19] Higashiwaki M., Sasaki K., Murakami H., Kumagai Y., Koukitu A., Kuramata A., Masui T., and Yamakoshi S. (2016). Recent Progress in Ga_2O_3 Power Devices. *Semiconductor Science and Technology 31(3)*. doi:10.1088/0268-1242/31/3/034001.

[20] Dai, Z. R., Pan, Z. W., and Wang, Z.L (2003). Novel Nanostructures of Functional Oxides Synthesized by Thermal Evaporation. *Advanced Functional Materials 13(1)*. doi:10.1002/adfm.200390013.

[21] Sun, X., and Li, Y. (2004). Ga_2O_3 and GaN Semiconductor Hollow Spheres. *Angewandte Chemie International Edition 43*. doi:10.1002/anie.200353212.

[22] Fleischer, M., and Meixner, H (1998). Selectivity in High-Temperature Operated Semiconductor Gas-Sensors. *Sensors and Actuators B: Chemical 52*. doi:10.1016/S0925-4005(98)00271-8.

[23] Pearton, S. J., Yang, J., Cary, P. J., Ren, F., Kim, J., Tadjer, M. J., and Mastro, M. (2018). A Review of Ga_2O_3 Materials, Processing and Devices. *Applied Physics Reviews 5*. doi:10.1063/1.5006941.

[24] Varley, J. B., Weber, J. R., Janotti, A., and Van de Walle, C. G. (2010). Oxygen Vacancies and Donor Impurities in *β*-Ga_2O_3. *Applied Physics Letters 97*. doi:10.1063/1.3499306.

[25] Zacherle, T., Schmidt, P. C., and Martin, M. (2013). *Ab-Initio* Calculations on the Defect Structure of *β*-Ga_2O_3. *Physical Review B 87*. doi:10.1103/PhysRevB.87.235206.

[26] Lyons, J. L. (2018). A Survey of Acceptor Dopants for *β*-Ga_2O_3. *Semiconductor Science and Technology 33(5)*. doi:10.1088/1361-6641/aaba98.

[27] Varley, J. B., Janotti, A., Franchini, C., and Van de Walle, C. G. (2012). Role of Self-Trapping in Luminescence and *p*-Type Conductivity of Wide-Band-Gap Oxides. *Physical Review B*. doi:10.1103/PhysRevB.85.081109.

[28] Lyons, J. L., Janotti, A., and Van De Walle, C. G. (2014). Effect of Hole Localization on Limiting *p*-Type Conductivity in Oxide and Nitride Semiconductor. *Journal of Applied Physics 115*. doi:10.1063/1.4838075.

[29] Zhang, K., Xi, K., Blamire, and M., Egdell, R. (2016). *P*-Type Transparent Conducting Oxides. *Journal of Physics: Condensed Matter 28(38)*. doi:10.1088/0953-8984/28/38/383002.

[30] Sabino, F. P., Wei, S. H., and Janotti, A. (2019). Enabling Visible-Light Absorption and *p*-Type Doping in In_2O_3 by Adding Bi. *Physical Review Materials 3*. doi:10.1103/PhysRevMaterials.3.034605.

[31] Sabino, F. P., Cai, X., Wei, S. H., and Janotti, A. (2019). Bismuth-Doped Ga_2O_3 as Candidate For *p*-Type Transparent Conducting Material. ArXiv:1906.00840v.

[32] Sabino, F. P., Nunes de Oliveira, L., and Da Silva, J. (2014). Role of Atomic Radius and *d*-States Hybridization in the Stability of the Crystal Structure of M_2O_3 (*M*=Al, Ga, In) Oxides. *Physical Review B 90*. doi:10.1103/PhysRevB.90.155206.

[33] Jain, A., Ong, S. P., Hautier, G., Chen, W., Richards, W. D., Dacek, S., Cholia, S., Gunter, D., Skinner, D., Ceder, G., Persson, K. (2013). Commentary: The Materials Project: A Materials Genome Approach to Accelerating Materials Innovation. *APL Materials 1*. doi:10.1063/1.4812323.

[34] Momma, K., and Izumi, F. (2011). *Vesta 3* for Three-Dimensional Visualization of Crystal, Volumetric, and Morphology Data. *Journal of Applied Crystallography 44*. doi:10.1107/S0021889811038970.

[35] Freysoldt, C., Neugebauer, J., and Van de Walle, C. G. (2010). Electrostatic Interactions Between Charged Defects in Supercells. *Physica Status Solidi B 248(5)*. Doi:10.1002/pssb.201046289.

[36] Peelaers, H., Varley, J. B., Speck, J. S., and Van de Walle, C. G. (2018). Structural and Electronic Properties of Ga_2O_3-Al_2O_3 Alloys. *Applied Physics Letters 112*. doi:10.1063/1.5036991.

[37] Wang, X., Liu, T., Lu, Y., Li, Q., Jiao, X., and Xu, X. (2019). Thermodynamics of Intrinsic Defects in β-Ga_2O_3. *Journal of Physics and Chemistry of Solids 132*. doi:10.1016/j.jpcs.2019.04.014.

[38] Chernyak, L. and Cahen, D. (2001). Controlled Ion Migration Tuning of Semiconductor Electrical Properties. *Defect and Diffusion Forum 191*. doi:10.4028/www.scientific.net/DDF.191.61.

[39] Gake, T., Kumagai, Y., and Oba, F. (2019). First-Principles Study of Self-Trapped Holes and Acceptor Impurities in Ga_2O_3 Polymorphs. *Physical Review Materials 3*. doi:10.1103/PhysRevMaterials.3.044603.

[40] Higashiwaki, M., and Jessen, G. (2018). Guest Editorial: The Dawn of Gallium Oxide Microelectronics. *Applied Physics Letters 112*. doi:10.1063/1.5017845.

[41] Sasaki, K., Kuramata, A., Masui, T., Víllora, E. G., Shimamura, K., and Yamakoshi, S. (2012). Device-Quality β-Ga_2O_3 Epitaxial Films Fabricated by Ozone Molecular Beam Epitaxy. *Applied Physics Express 5(3)*. doi:10.1143/apex.5.035502.

[42] Guo, Z., Verma, A., Wu, X., Sun, F., Hickman, A., Masui, T., Kuramata, A., Higashiwaki, M., Jena, D., and Luo, T. (2015). Anisotropic Thermal Conductivity in Single Crystal β-Gallium Oxide. *Applied Physics Letters 106*. doi:10.1063/1.4916078.

[43] Santia, M. D., Tandon, N., and Albrecht, J. D. (2015). Lattice Thermal Conductivity of β-Ga_2O_3 From First Principles. *Applied Physics Letters 107*. doi:10.1063/1.4927742.

[44] Mu, S., Peelaers, H., and Van de Walle, C. G. (2019). *Ab-Initio* Study of Enhanced Thermal Conductivity in Ordered $AlGaO_3$ Alloys. *Applied Physics Letters 115*. doi:10.1063/1.5131755.

[45] Hudgens, J. L., Simin, G. S., Sanit, E., and Khan, M. A. (2003). An Assessment of Wide Bandgap Semiconductors for Power Devices. *IEEE Transactions on Power Electronics 18(3)*. doi:10.1109/TPEL.2003.810840.

[46] Slack, G. A. (1972). Nonmetallic Crystals with High Thermal Conductivity. *Journal of Physics and Chemistry of Solids 34(2)*. doi:10.1016/0022-3697(73)90092-9.

[47] Shannon, R. D. (1976). Revised Effective Ionic Radii and Systematic Studies of Interatomic Distances in Halides and Chalcogenides. *Acta Crystallographica A32*. doi:10.1107/S0567739476001551.